SAND2013-10764C

Structure and stabilization of hydrogen-rich transverse jets in a vitiated turbulent flow

S. Lyra[1], B. Wilde[2], H. Kolla[1], T.C. Lieuwen[2] & J.H. Chen[1]

[1] *Reacting Flow Research Department, Combustion Research Facility, Sandia National Laboratories Livermore, CA 94551, USA*

[2] *School of Aerospace Engineering, Georgia Institute of Technology Atlanta, GA 30332, USA*

Abstract

Fuel rich hydrogen transverse jets in high temperature vitiated fully developed turbulent channel flow under inert and chemically reacting conditions are studied in a joint experimental and numerical approach. Simultaneous stereoscopic PIV, OH-PLIF, three-dimensional dynamic pressure measurements and results from direct numerical simulations with detailed H_2/CO-air chemistry are reported. The paper investigates the effects of the elevated temperature, composition and broadband turbulence of the vitiated cross-flow on the transverse jet, the mixing and flow field, flame stabilization, structure and combustion mode. The three dimensional DNS results of the inert and reacting JICFs show good agreement with the measured mean velocity fields. The mean flame location demarcated by the OH concentration is well captured. Instantaneously, the inert and reacting shear layers are unstable, characterized by the formation of Kelvin-Helmholtz vortical structures responsible for the fuel-oxidant mixing. In the inert JICF the vortex roll-up has a pronounced preferred shedding frequency, whereas the shedding is more broadband when reactions are initiated. Dilatational effects induced by the density drop in the presence of the flame are important contributors to the increased jet width. Frequency spectra of the span-wise vorticity at distinct locations suggest that the shear layer instability corresponds to a Strouhal number of 0.69 and that the reacting jet is convectively unstable. The propensity of the mixture to ignite prior to ignition and the global structure of the resultant burner attached diffusion flame is investigated using both CEMA and the Takeno flame index. The mixture is highly explosive prior to ignition and after reactions are activated, a diffusion flame establishes anchored at the stagnation point in the wind-ward side and at the low velocity region in the lee-ward side.

Keywords: DNS, experiment, transverse jet, vitiated cross-flow.

1. Introduction

The transverse jet in cross flow (JICF) is a versatile configuration employed in many industrial and transportation combustion systems. It facilitates rapid mixing between two streams in a compact volume, driven primarily by a complex three-dimensional flow field [1], and can be very effective in systems where size is a constraint. In particular it is widely encountered in gas turbine combustors both in aircraft engines as well as industrial power plants. With emerging gas turbine technologies increasingly favoring lean premixed combustion, the JICF is growing ever more ubiquitous both in fuel nozzles and the combustor itself. For instance the lean-premixed-prevaporized (LPP) concept of aircraft engine combustor relies on a JICF type fuel injector to quickly mix the vaporized liquid fuel with gaseous air. Likewise, industrial gas turbine combustors operating with natural gas or hydrogen-rich gaseous fuels employ a JICF based fuel premixer. In both these applications the JICF provides rapid mixing to enable the primary combustion zone to operate in a lean premixed mode.

The JICF is also used in staged combustors in both aircraft and stationary gas turbines where either an air jet mixes with a rich, vitiated crossflow, or a secondary fuel jet issues into lean combustion products from a primary combustion zone. Fuel staging is an attractive design strategy as it can facilitate fuel flexibility and enable load variations whilst satisfying stringent emission regulations. However, for fuel premixing the JICF near field flame stabilization is important to intrinsic flashback safety (i.e., to ensure that a flame cannot stabilize in the JICF wake if it were to flashback), while for staged combustion, the design concern is primarily that of temperature uniformity into the turbine, NO_x emissions from the secondary zone, and JICF thermoacoustics.

The fundamental momentum and scalar transport in non-reacting JICF has been studied extensively both experimentally and numerically. Comprehensive recent reviews are given by Mahesh [2] and Karagozian [3]. Previous work has focused primarily on the influence of momentum flux ratio, density ratio, nozzle geometry, Reynolds number, and boundary layer thickness in inert JICF configurations [1, 4–7]. Much less is known, however, about the behavior of reacting JICF, particularly at cross flow temperatures relevant in practical devices. Near field flame stabilization in moderate temperature cross flow was studied experimentally by [8] and using direct numerical simulations by [9, 10]. Higher temperature cross flows were recently studied experimentally by [11–13], which show that auto-ignition in the near field can play an important role in flame stabilization for high temperature cross flows. The work presented here extends those previous studies in order to better understand flame stabilization characteristics in vitiated crossflows and explores the effect of near field heat release on jet dynamics.

This paper presents the first set of results from a joint experimental-numerical investigation of a hydrogen-rich jet in a vitiated cross flow comprised of products of methane combustion, using complementary information from experiments and direct numerical simulations (DNS). The near field flame stabilization is also of interest and in particular the role of auto-ignition which might become even more prominent since the cross flow, in addition to being at high temperature, contains a small amount of radicals. We report flame characteristics and stabilization mechanisms that are quite distinct from those observed in previous JICF studies. These will invariably influence the fluid dynamics, particularly the near field shear layer instabilities and growth rates, the jet/crossflow mixing, the heat release distribution, and thermoacoustics.

The paper is structured as follows. Section 2 describes the experimental facility at and the diagnostics used in the experiment. Section 3 describes the direct numerical simulation (DNS) code and the physical and numerical parameters of the configuration. Comparison of the experimental data and the DNS results are given in Section 4. Finally, the main findings and conclusions drawn from the analysis are summarized in Section 5.

2. Experimental Facility and Diagnostics

Two test conditions are considered in the present work, one reacting and one non-reacting. The experimental facility utilized for both conditions is comprised of three sections: i) a vitiator, ii) a flow conditioning section, and iii) an optically accessible test section. A schematic of the facility is shown in Figure 1. The vitiator section consists of a swirl-stabilized, partially-premixed natural gas burner coupled to a cylindrical, refractory-lined combustion chamber. In the reacting case, the vitiator is operated at an overall equivalence ratio of $\Phi = 0.46$.

Hot product gases from the vitiator expand into the rectangular flow conditioning section and opposed air inlets inject a metered quantity of room-temperature dilution air to reduce the temperature of the vitiated products to $T \sim 1200\,\mathrm{K}$. A series of settling chambers and flow straighteners condition the crossflow such that nominally fully-developed turbulent channel flow is supplied to the test section, where the jet is injected flush with the lower wall. Reynolds number of the crossflow in the test section based on mean velocity and channel height for the reacting and non-reacting conditions is $Re_o = 9480$ and $Re_o = 40200$, respectively.

The test section dimensions are 127 mm x 76.2 mm and optical access is provided by quartz windows at the top and sides of the test section. The jet is injected normal to the crossflow direction $86\,d_j$ downstream of the entrance to the test section. The jet injector is fabricated from ceramic to minimize quenching and its contour is identical to that used at UCLA [14]. The smooth contraction nozzle generates a thin, nearly tophat velocity profile at the exit.

The jet composition is 70% H_2/30% He by volume for the reacting case and 28% N_2/72% He for

the non-reacting. The jet enters the test section at $T \sim 300\,\mathrm{K}$ in both cases. Jet-to-crossflow density ratio, $S = \rho_j/\rho_\infty$, is 0.37 based on the mean jet and crossflow density. The jet-to-crossflow momentum flux ratio, $J = \rho_j {u_j}^2/\rho_\infty u_\infty^2$, is 9 and the jet Reynolds number based on mean jet velocity is $Re_j = 2420$.

The jet fluid passes through a choked orifice 40 d_j upstream of the jet injection location to minimize injector coupling between the crossflow acoustics and the jet supply system. Crossflow acoustics during tests are characterized using Kistler 211B6 sensors in a two-microphone method configuration. A third Kistler sensor is located in the jet supply plenum. Finally, the vitiator has been carefully tuned to achieve the lowest possible crossflow acoustics, whose associated flow oscillations are approximately 1% of the crossflow velocity and less than 0.2% of the jet velocity.

Simultaneous high-speed stereoscopic particle image velocimetry (SPIV) and OH planar laser induced fluorescence (OH-PLIF) were used to characterize the flowfield. Illumination was provided by a dual head, frequency doubled Nd:YLF laser (Litron LDY303-HE) operated at 10kHz, with measured pulse energy of about 2 mJ. The laser beam was expanded, collimated, formed into a ~ 1 mm thick sheet, and guided into the test section using a series of mirrors and converging/diverging lenses (LEO) suspended above the test section. The laser sheet was aligned to the jet centerplane, and the laser pulses for the non-reacting and reacting cases were separated by $9.00\mu s$ and $3.70\mu s$, respectively.

SPIV images were captured by two Photron SA5 cameras mounted in a side-scatter configuration. The cameras were positioned approximately 30° relative to the jet centerplane normal coordinate (z-axis). Each camera was equipped with a 105 mm focal length Tokina lens at $f/8$ mounted on Scheimpflug adapters and viewed the test section through a Semrock Brightline 527/20 filter. Standard corrections for perspective and distortion were made using a LaVision 058-5 3D dot target. Camera resolution was 512 x 512 and the viewable area was approximately 45 mm square. 11,000 double-framed images were recorded at each test condition ($\sim 1.1s$).

Both the crossflow and the jet were seeded with Dupont R-960 TiO_2 particles with mean particle diameter of $0.50\mu m$. The crossflow seeding system consisted of a passively agitated swirling seeder operated with about 1 g/s of air flow, while the jet flow was seeded using a small surface spray type seeder. Seeded crossflow air was injected through the dilution air ports. Seeding density of the crossflow and the jet were manually balanced. Velocity vectors were computed using LaVision DaVis 8.1.6 software with multi-pass processing and adaptive interrogation windows. Initial interrogation windows were 24 x 24 with 50% overlap while final interrogation windows were 16 x 16 with 75% overlap, resulting in vector spacing of about 0.35 mm.

The high-speed OH-PLIF system consisted of a frequency doubled Nd:YAG laser (Edgewave InnoSlab IS811-E) with output power of 40W pumping a tunable dye laser (Sirah Credo LG24). The UV output at approximately 283 nm had pulse width of about 9ns and pulse energy of 0.2 mJ. The dye laser wavelength was tuned to the $Q_1(9)$ transition of OH in the $(0,1)$ band of the $A^2\Sigma^+ - X^2\Pi$ system. The UV laser beam was expanded, collimated, and combined with the SPIV sheet. Both laser sheets were approximately 50 mm wide. The OH-PLIF laser sheet was focused to a thickness of about 0.4 mm.

The fluorescence signal near 310 nm was collected using a Photron SA1.1 camera optically coupled to a Lambert Instruments HiCatt 25 intensifier and a 45 mm Cerco $f/1.8$ lens. The OH-PLIF camera was located in between the SPIV cameras and normal to the jet centerplane. The intensifier was gated to 200 ns and the timing of the cameras and lasers for both systems were controlled using a BNC Model 575 timing unit. Background flame luminescence was blocked using a narrow-band interference filter. 9,700 images were recorded per OH-PLIF data set and the resolution was 768 x 768. Viewable area was similar to that of the SPIV and standard corrections for perspective and distortion were applied using images of the 3D target. Laser sheet intensity variations along the x-direction were corrected using an acetone calibration procedure, and the final OH-PLIF images were corrected for background OH, which was generally very low (< 10 counts).

3. Mathematical Description and Configuration

The DNS are performed using the code S3D [15] which solves the compressible formulation of continuity, Navier-Stokes, total energy and species conservation equations on a structured 3D Cartesian grid using explicit eighth-order centered finite difference scheme for spatial derivatives and a fourth-order, six-stage explicit Runge-Kutta scheme for time advancement. S3D implements finite rate chemical kinetics and mixture averaged transport coefficients by interfacing with CHEMKIN and TRANSPORT libraries [16, 17]. The chemical reactions in the gas phase are described by a detailed mechanism for H_2/CO combustion [18], involving 13 species and 35 reactions. Nitrogen is assumed to be inert and NO_x formation reactions are not considered. The extent of the computational domain is $45mm \times 44.5mm \times 44.5mm$ in the stream-wise (x), transverse (y) and span-wise directions (z), respectively. Navier-Stokes characteristic boundary conditions (NSCBC) are imposed and the stream-wise boundaries are treated as non-reflecting inflow and outflow, while the span-wise boundaries are specified as periodic. The transverse boundaries are treated as adiabatic, no-slip, inert walls. A transverse jet of diameter, $d_j = 1.5mm$ issues vertically from the lower boundary and its centre is located at 5.5 mm from the upstream x boundary at the span-wise mid-plane. The cross-flow corresponds to a fully developed turbulent

channel flow comprised of combustion products of natural gas.

Figure 2 presents the DNS configuration from instantaneous volume renderings of H_2O and H_2 mass fractions and temperature. The jet and cross-flow compositions and the physical and numerical parameters have been selected so that the jet and cross-flow Reynolds numbers, the momentum flux, the density ratio and Damköhler number are identical with the experiment. To ensure that the Damköhler number, defined based on jet time-scale and ignition time scale of stoichiometric mixture, matches that of the experiment, the jet and cross-flow temperatures have been adjusted to 407.26 K and 1640 K, respectively. Unlike in JICFs of moderate air temperature cross-flows where a lifted flame is anchored on the jet lee-ward side where low prevailing velocities create stoichiometric mixtures and sufficient residence times for reactions to occur, here, the elevated temperature vitiated channel flow leads to small ignition delay times. This, in turn, promotes the establishment of an anchored flame as soon as the fuel issues from the nozzle tip and mixes with the crossflow. The significant concentration of H_2O around the jet in the near field denotes the development of a stable flame that encompasses the fuel plume and spans both in the wind-ward and lee-ward jet sides.

The time-dependent fluctuating velocity field imposed at the inflow boundary is obtained from an auxiliary inert fully developed turbulent channel flow simulation. The auxiliary channel flow simulation is performed on a domain that is $178.3mm \times 44.5mm \times 44.5mm$ in the x, y and z directions, respectively and with a grid of $1000 \times 720 \times 240$ points. The grid spacing is uniform in the x and z directions while it is refined in the y direction to ensure that the near-wall boundary layer is sufficiently resolved, with the first point located at $y^+ \sim 0.25$, and 30 points below $y^+ \sim 10$. The inert simulation is run for five flow through times, based on the centerline velocity, before it is deemed as fully developed. The inert JICF simulation is initially performed for one flow through time that allows for the hydrogen plume to be established. Subsequently the inert JICF solution is advanced for three more flow through times. In parallel, a reacting JICF DNS is performed in which the plume is ignited and the simulation is advanced at an intermediate resolution so that the ignition transient is flushed out of the computational domain. The solution is then up-sampled to the production grid with $1500 \times 2080 \times 1500$ points in the x, y and z directions, respectively. The calculations are performed on Titan at ORNL and Edison at NERSC on more than 10^5 cores.

4. Results and Discussion

Reynolds-averaged flame and flow features on the span-wise mid-plane of the inert and reacting JICF are presented in Fig.3 and 4 respectively. Note that the velocity is not well-resolved below $y/d = 0.75$ in the experiment due to laser reflections off the lower wall. The figures compare averaged velocity magnitude and OH mass fraction fields on the span-wise mid-plane. The mean heat release rate iso-lines, spanning 10% to 90% of the maximum, are super-imposed on the DNS results to demarcate the reaction zone. The major flow and flame features such as jet trajectory, spreading rate and flame brush extent are qualitatively similar between the DNS and experiment. In particular, the presence of significant heat release rate on the jet wind-ward side shows that a thin reaction zone is formed in the mixing layer between the cross-flow and the jet near field that leads to an attached flame established near the jet exit. The peak volumetric heat release rate occurs at approximately $y/d \sim 0.75$, within a region where the average mixture fraction is nearly stoichiometric $\bar{\xi} = 0.04$, ($\bar{\xi}_{st} = 0.03$), at the outer edge of the jet shear layer (the vorticity magnitude is $\sim 2\%$ of the maximum value) where the average velocity is relatively low, $\bar{U}/u_j \sim 10\%$. On the lee-ward side of the jet a broader reaction zone is observed where the mean volumetric heat release rate is lower than the peak volumetric heat release rate observed on the wind-ward side by as much as a factor of 10. This is due to the lower gradients in the non-premixed flame (discussed further below). However, this does not imply that the total heat release of the lee-ward side flame is substantially lower - rather the volumetric heat release rate is lower, but occurs over a larger volume. The lee-ward flame branch is located in a low velocity, and thus low strain rate, region characterized by long residence times where the mean OH concentration and temperature (not shown) fields reach their maximum levels. Note that the two flame branches remain firmly attached to the burner outlet at all times, and detachment from the wall was not observed in either the experiment or the simulation. The low velocity region formed in the jet lee-ward side at $x/d \sim 4$ and $y/d \sim 2$ in the inert JICF persists for reacting conditions.

It is noteworthy that the mean flame characteristics observed here are considerably different than those of the non-vitiated cross-flow case of Grout *et al.* [9], which were studied using the same DNS code and methodology. In the latter, the flame was anchored on the jet lee-ward side where a low velocity region coincided with near stoichiometric mixture conditions. No distinct wind-ward flame branch was observed (a lifted wind-ward branch, presumably due to propagation of the flame from the lee-ward side stabilization point around the jet, was reported from experiments in [8]). Furthermore, intense turbulent mixing in the near field was critical in enabling partially premixed flame stabilization near the anchoring location, and a slight modification in conditions disrupted the flame anchoring resulting in blow-off [10]. In contrast, under the current vitiated conditions, the flame is uniformly stabilized adjacent to the jet exit over its entire circumference.

Fig. 5 presents scatter plots, on the jet wind-ward and lee-ward sides separately, of the heat release rate against the local mixture fraction in the near field

($y/d < 3$). Also shown are one-dimensional laminar flame results, obtained using OPPDIF [20], corresponding to a low strain rate ($500\ 1/s$) and a very high strain rate ($17,000\ 1/s$). Consistent with Fig. 4, the scatter plot reveals that the maximum heat release rate occurs at near stoichiometric conditions on both sides of the jet. Furthermore, the heat release rate with respect to the mixture fraction is broadly distributed on the wind-ward side, exhibiting large conditional fluctuations which suggests that the flame behavior in the vicinity of the wind-ward near field may not be flamelet-like. On the contrary, the narrow distribution of the heat release on the lee-ward flame branch would suggest that the flame could be parametrized by a mixture fraction based manifold. The conditional mean and rms mixture fraction scalar dissipation rate in phase space on the wind-ward and lee-ward jet sides are presented in Fig. 5 (right). The mean scalar dissipation rate is comparable on both jet sides, although it is slightly higher on the lee-ward side. The rms of the conditional scalar dissipation is higher on the windward jet side, which suggests that the higher heat release rate levels, compared to the lee-ward side, are possibly due to higher strain rates, consistent with one-dimensional laminar flame results.

The strong density gradients and flow dilatation occurring near the reaction zone raises important questions regarding the dynamics of the well-known coherent vortical structures of the JICF, which are thought to control important JICF processes such as mixing and penetration [3]. Figure 6 shows the instantaneous span-wise vorticity component from the inert and reacting JICFs and reveals the characteristics of the complex interaction process between the cross-flow and the transverse jet. Iso-lines of the instantaneous OH mass fraction are superimposed to identify the flame location in the reacting case (again, note the significantly different thickness of the reaction zone on the lee-ward and wind-ward side, as inferred from these OH contours). The instantaneous vorticity fields, both from the experiment and the DNS, indicate the formation and growth of the shear layer which rolls up into concentrated regions of vorticity and amalgamate with downstream distance. Note that the relatively low dynamic range of macroscopic high-speed SPIV ($O(100)$) results in noisy instantaneous vorticity contours from the experiment. While the instability of the shear layer is evident in both inert and reacting conditions, in the absence of the flame the vortex roll-up is strongly periodic. In the reacting case, however, the shear layer roll-up is strongly modified in regions where chemical reactions dominate and does not exhibit periodicity. Vortex pairing occurs earlier in the presence of the flame and the jet width is significantly enhanced as a result of the increased rate of cross-flow fluid entrainment [7, 21] and gas expansion due to the chemical reactions. The size of the paired structures in the reacting cases, particularly evident at locations $y/d > 2$, are significantly larger than in the non-reacting cases. This may be due to effects of density inhomogeneities on the wavelength of maximum amplification of the Kelvin-Helmholtz instability, as well as gas dilatation effects. Fig. 7 illustrates the dilatation effects by comparing the Reynolds averaged span-wise vorticity component from the inert and reacting JICFs. The OH mass fraction iso-lines denote the mean flame location with respect to the shear layer in the jet near field. Compared to the inert results, span-wise vorticity fields exhibit increased spreading under reacting conditions, a finding which is observed both in the DNS and the experiment. The density reduction as a result of the chemical reactions enhances the mean engulfment of packets of fluid from the cross-flow to the jet, by the large vortical structures formed at $y/d > 2$, thus contributing to the observed enhanced mean shear layer growth rate.

The span-wise vorticity in the wind-ward shear layer of the reacting JICF is sampled during the simulation at two distinct locations in order to explore the unsteady dynamics of the wind-ward shear layer, which may be critical to understanding the observed differences in shear layer growth rate. The first probe is placed at ($x/d = 2.9$, $y/d = 1$), and the second probe is placed at ($x/d = 3.8$, $y/d = 3$). The simulation data is uniquely capable for this task since the Nyquist frequency associated with the 10 kHz SPIV measurements limits their usefulness to $St \leq 0.17$. The frequency spectra from the two probes are shown in Fig. 8. Clearly two distinct modes can be identified from the first probe. The most prominent mode is at $\sim 69KHz$ which corresponds to a Strouhal number of 0.36 and the next dominant mode is at $\sim 133KHz$ (Str=0.69). The high frequency mode corresponds well to the expected shear layer instability frequency seen in previous work [22, 23] on non-reacting JICF, whereas the lower one is likely a subharmonic. Conversely, the frequency spectrum at the second probe location, which is further downstream, is significantly broader, features more modes, and exhibits much less concentrated spectral energy. The significant difference in the shear layer spectra at two closely positioned probes in the wind-ward shear layer suggests that the reacting JICF may be convectively unstable rather than globally unstable. This result is in contrast to the non-reacting JICF literature but is consistent with the observation that the shear layer roll-up in the reacting case loses the pronounced periodicity seen in the non-reacting case.

To identify the mode of combustion and the flame stabilization mechanism the DNS data is processed using the chemical explosive mode analysis (CEMA). CEMA is a useful diagnostic that can systematically detect limit flame phenomena, e.g. local ignition and extinction, and premixed flame fronts [24]. A chemical explosive mode (CEM) is the eigenmode associated with the largest eigenvalue of the Jacobian of the chemical reaction rates, with a positive real part. The distribution of the chemical explosive mode (t_{exp}), is shown in Fig. 9 at the span-wise mid-plane from the inert and reacting DNS, at one instant. In the inert case fast chemical modes are present in the near

jet field, encompassing both the wind-ward and the lee-ward sides. The cross flow, comprised of burnt products in equilibrium and thus exhibits negative explosive modes since it is non-ignitable. In contrast, in the reacting case a flame envelope immediately forms around the jet and anchors at the nozzle tip, and the flame front is characterized by a negative explosive mode (t_{exp}), indicating an almost instantaneous transition to burnt conditions. The dark blue zones ($t_{exp} << 0$) indicate the strong diffusion flame branches, in which reactions take place, but the mixture would not proceed to thermal runaway in isolation. Two thin islands demarcated in red ($t_{exp} >> 0$) in the wind-ward shear layer correspond to auto-ignitive fuel-oxidizer mixtures created by the shear layer vortices. To further examine the nature of the flame, a local Damköhler number defined as $Da = sign(t_{exp}) \times \log_{10}[max(1, |t_{exp} \cdot \omega^{-1}|)]$ where $|\omega|$ is the vorticity magnitude, is shown on the span-wise mid-plane in Fig 10. Values of $Da << 1$ are associated with the slowest decaying mode in a non-explosive mixture. The local Da within the region surrounding the jet is $\sim$ 7, indicating that the chemistry occurs faster than mixing, and thus the flame is mixing-limited.

The Takeno flame index [25] defined as $FI = \frac{\nabla Y_F \cdot \nabla Y_{Ox}}{|\nabla Y_F| \cdot |\nabla Y_{Ox}|}$, where subscripts F and Ox denote the fuel and oxidizer, is a useful tool for analyzing the nature of the flame; the flame index is +1 in purely premixed and -1 for diffusion flames, respectively. The flame index and the iso-lines of heat release shown in Fig. 10 illustrate that the fuel and oxidizer gradients are misaligned in regions where chemical reactions prevail therefore defining a diffusion combustion mode. Unlike in flames stabilized in moderate temperature cross-flow where partially premixed combustion takes place, in the present JICF combustion occurs primarily in the diffusion mode. Statistical results confirm that 70% of the combustion occurs under conditions in which the alignment between fuel and oxidizer gradients exceeds 115^o.

5. Conclusions

This paper presents a joint experimental and numerical investigation of inert and reacting hydrogen rich laminar transverse jets in vitiated fully developed turbulent channel flows. The DNS results in the inert and reacting JICFs show good agreement with the measured mean velocity fields. The mean flame location demarcated by the OH concentration is well captured. Both the inert and reacting shear layer are unstable and rolls up into concentrated vortices which are responsible for the fuel-crossflow mixing. In the absence of reactions, the vortex spacing is uniform, a uniformity which does not exist in the reacting case. Frequency spectra of the span-wise vorticity at distinct locations suggest that the shear layer instability corresponds to a Strouhal number of 0.69 and that the reacting jet is convectively unstable. Chemical reactions are found to enhance the rate of radial jet spreading. The propensity of the mixture to ignite prior to ignition and the global behavior of the formed diffusion flame is investigated using both CEMA and the Takeno flame index. The mixture is highly explosive prior to ignition and after reactions are activated a diffusion flame establishes anchored at the stagnation point on the wind-ward side and at the low velocity region on the lee-ward side.

6. Acknowledgements

The work at Sandia National Laboratories was sponsored by the US Department of Energy, Office of Basic Energy Sciences, Division of Chemical Sciences, Geosciences, and Biosciences. The research used resources of the OLCF at Oak Ridge National Lab, & the National Energy Research Scientific Computing Center. The authors would also like to thank Prof. Ann Karagozian for generously sharing the contoured nozzle profile used in this work. The authors are grateful for the invaluable assistance of Ianko Chterev during setup of the diagnostic hardware.

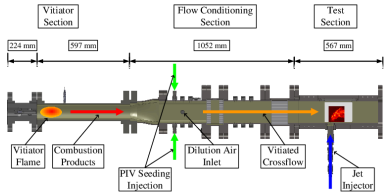

Fig. 1: Schematic of the Reacting JICF Facility

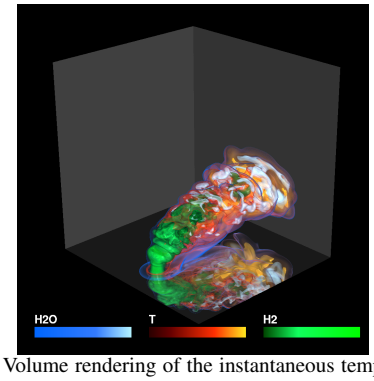

Fig. 2: Volume rendering of the instantaneous temperature, H_2O and H_2 mass fraction fields.

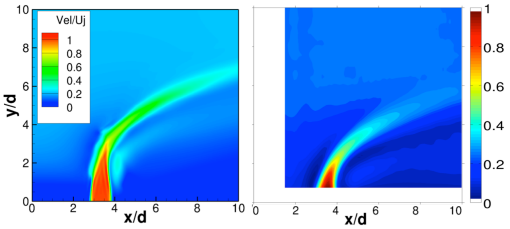

Fig. 3: Reynolds-averaged velocity magnitude normalized by u_j from the inert JICF, left: DNS, right: experiment.

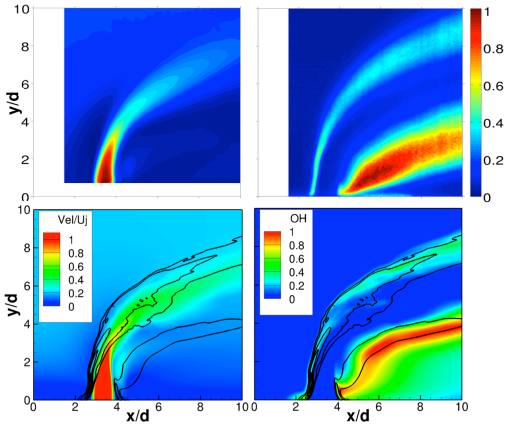

Fig. 4: Reynolds-averaged velocity magnitude normalized by u_j (left) and normalized OH mass fraction (right), top: experiment, bottom: DNS from the reacting JICF. Iso-lines of the mean heat release rate between $10\% - 90\%$ (black) are overlaid on the DNS.

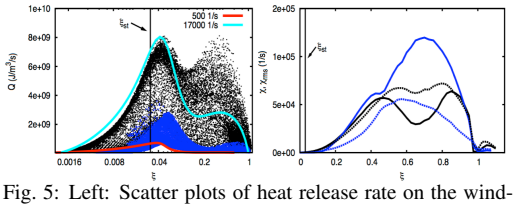

Fig. 5: Left: Scatter plots of heat release rate on the wind-ward (black) and lee-ward (blue) sides. The stoichiometric mixture fraction is denoted with the black line. The lines denote laminar strained flames at 500 1/s and 17,000 1/s, respectively. Right: Conditional mean (solid lines) and rms (dashed lines) of the mixture fraction scalar dissipation rate on the wind-ward (black) and lee-ward (blue) sides of the jet.

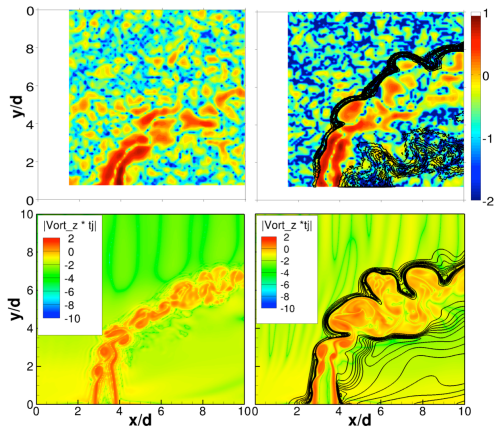

Fig. 6: Logarithm of the span-wise vorticity component normalized by $t_j = d_j/u_j$ from the inert (left) and reacting (right) JICF, top: experiment, bottom: DNS. Iso-lines of the OH mass fraction between $10\% - 90\%$ of the maximum (black) demarcate the flame location.

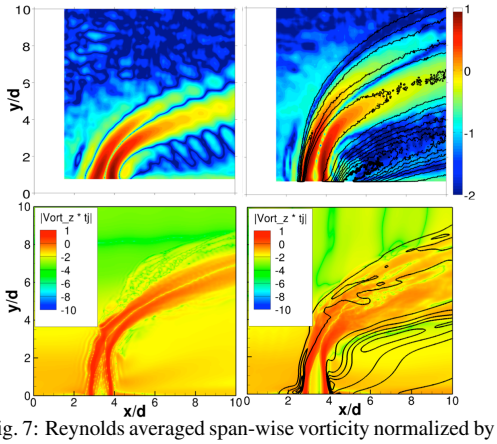

Fig. 7: Reynolds averaged span-wise vorticity normalized by $t_j = d_j/u_j$ from the inert (left) and reacting (right) JICF, top: experiment, bottom: DNS. Iso-lines of the mean OH mass fraction between $10\% - 90\%$ of the maximum (black) demarcate the flame location.

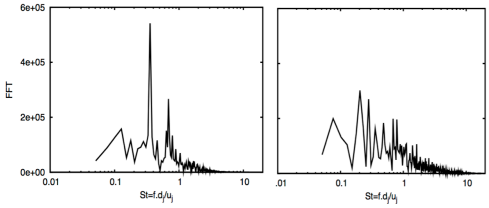

Fig. 8: Frequency spectra from probes 1 (left) and 2 (right).

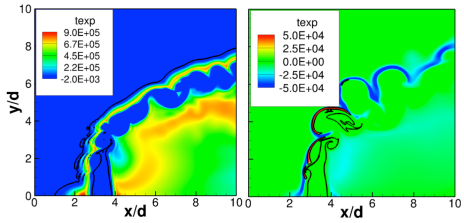

Fig. 9: Chemical explosive mode (t_{exp}) at the span-wise mid-plane from the inert (left) and reactive (right) DNS. The boundary between non-explosive and explosive regions is delineated by a black iso-contour at $t_{exp} = 0$.

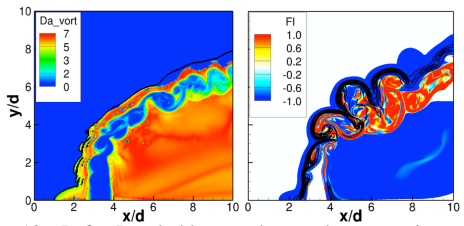

Fig. 10: Left: Damköhler number at the span-wise mid-plane from the inert DNS. Right: Takeno flame index from the reacting DNS. Iso-lines of the heat release rate, between 20%-80% of the peak (black) demarcate the reaction zone.

References

[1] T. F. Fric, A. Roshko, *J. Fluid Mech.* 279 (1994) 1 – 47.

[2] K. Mahesh, *Ann. Rev. of Fluid Mech.* 45 (1) (2013) 379–407.

[3] A. R. Karagozian, *Prog. in Energy and Comb. Sci.* 36 (2010) 531–553.

[4] S. Muppidi, K. Mahesh, *Phys. Fluids* 18 (2006) 085103–1 – 085103–9.

[5] S. Muppidi, K. Mahesh, *J. Fluid Mech.* 574 (2007) 59 –84.

[6] M. Salewski, D. Stankovic, L. Fuchs, *Turbulence Combust.* 80 (2008) 255 –283.

[7] E. Hasselbrink, M. Mungal, *J. Fluid Mech.* 443 (2001) 27 –68.

[8] A. M. Steinberg, R. Sadanandan, C. Dem, P. Kutne, W. Meier, *Proc. Comb. Inst.* 34 (2013) 1499 –1507.

[9] R. Grout, A. Gruber, H. Kolla, P. Bremer, J. Bennett, A. Gyulassy, J.H.Chen, *J. Fluid Mech.* 706 (2012) 351–383.

[10] H. Kolla, R. Grout, A. Gruber, J.H.Chen, *Combust. Flame* 159 (2012) 2255 –2766.

[11] D. Micka, J. Driscoll, *Combust. Flame* 159 (2012) 1205–1214.

[12] J. Fleck, P. Griebel, A. Steinberg, C. Arndt, M. Aigner, *Int. Jou. Hydrogen Energy* 38 (2013) 16441–16452.

[13] R. Sullivan, B. Wilde, D. R. Noble, K. Periagaram, J. M. Seitzman, T. C. Lieuwen, *Proc. Comb. Inst.*.

[14] S. Megerian, J. Davitian, L. de B. Alves, A. Karagozian, *J. Fluid Mech.* 593 (2007) 93–129.

[15] J. Chen, A. Choudhary, B. de Supinski et. al., *Comput. Sci. Discov.* 2 (1) (2009) 1–31.

[16] R. J. Kee, F. Rupley, E. Meeks, J. Miller, *Report No. SAND96-8216, Sandia National Laboratories, 1996*.

[17] R. J. Kee, G. Dixon-Lewis, J. Warnatz, M. Coltrin, J. Miller, *Report No. SAND86-8246, Sandia National Laboratories, 1986*.

[18] J. Li, Z. Zhao, A. Kazakov, F. Dryer, *Int. J. Chem. Kinet.* 36 (2004) 566 – 575.

[19] D. Han, M. Mungal, *Proc. Comb. Inst.* 29 (2002) 1889 –1895.

[20] A. Lutz, R. Kee, J. Grcar, F. Ruply, *Tech. Rep., SAND96-8243, Sandia National Laboratories*.

[21] L. Muñiz, M. Mungal, *Combust. Flame* 126 (1-2) (2001) 1402 – 1420.

[22] S. Bagheri, P. Schlatter, P. Schmid, D. S. D.S. Henningson, *J. Fluid Mech.* 624 (2009) 33–44.

[23] J. Davitian, D. Getsinger, C. Hendrickson, A. Karagozian, *J. Fluid Mech.* 661 (2010) 294–315.

[24] T. Lu, C. Yoo, J. Chen, C. Law, *J. Fluid Mech.* 652 (2010) 45–64.

[25] H. Yamashita, M. Shimada, T. Takeno, *Proc. Comb. Inst.* 26 (1996) 24 –34.